Performance of GNSS Evil Waveform Detectors in the Presence of Multipath

Fernando D. Nunes
Instituto de Telecomunicações
and Instituto Superior Técnico
Lisboa, Portugal
nunes@lx.it.pt

Fernando M. G. Sousa
Instituto de Telecomunicações
and Instituto Superior de Engenharia de Lisboa
Lisboa, Portugal
fsousa@isel.pt

2022 10th Workshop on Satellite Navigation Technology (NAVITEC) | 978-1-6654-1616-0/22/$31.00 ©2022 IEEE | DOI: 10.1109/NAVITEC53682.2022.9847550

***Abstract*—The detection of evil waveforms (EWF) in GNSS signals is crucial to refrain from using anomalous signals in the PVT solution, which could degrade significantly its accuracy. The EWF detectors are, in general, based on the computation of the distortion of the code autocorrelation function. Thus, the multipath effect, an independent mechanism that also distorts the autocorrelation shape, can be incorrectly assumed by the EWF detector as the presence of EWF, leading to a major increase of the probability of false alarm. In the paper we analyze the robustness of the main EWF detectors and modulations to the presence of multipath.**

***Index Terms*—evil waveform, multipath, threat models**

I. Introduction

Evil waveform (EWF) detection comprises algorithms to detect the presence of different types of distortion in the transmitted signals provoked by electric anomalies that occur in the signal generators aboard the GNSS space vehicles [1]-[4]. The processing of EWF distorted signals by the GNSS receiver may lead to a significant loss of accuracy in the PVT solution, thus preventing its utilization in most applications [5]. Three different types of EWFs are usually considered in the literature [1], [3]: threat models TM-A, TM-B and TM-C, which are associated with digital, analog and digital plus analog distortion, respectively.

According to [3], [7], the main EWF detection algorithms are based on three tests: T_1 (simple ratio), T_2 (difference ratio) and T_3 (sum ratio). These tests measure the distortion of the code autocorrelation shape, namely the flatness of the main peak or the correlation asymmetry. As such, they require the use of a bank of early/late correlators plus a central correlator aligned with the autocorrelation main peak.

Often the incoming signals are also affected by multipath which consists of receiving more than one replica of the transmitted signal with different delays and phases due to reflection in mountains, buildings, etc. Both effects, EWF and multipath, tend to distort the code autocorrelation function in a way that jeopardizes the identification of each effect. As a result, when EWF detection algorithms are used in the presence of multipath distorted signals, the probability of false alarm (P_{fa}) tends to increase significantly. Simulations have shown that the probability of missing detection (P_{md}) is also affected by the existence of multipath, although the changes are typically less important.

In this paper we analyze the robustness of the different EWF detectors to the presence of multipath. The following modulations are tested: BPSK, BOCs and CBOC pilot, which are currently used in GPS, Galileo and Beidou. As the probability of false alarm is prone to increase more significantly than the probability of missing detection in the presence of multipath, we propose to use a chain of physically separate receivers to minimize the degradation of performance, by taking into account the different statistical nature of the EWF and multipath events.

This work is funded by FCT/MCTES through national funds and when applicable co-funded by EU funds under the project UIDB/50008/2020

II. Signal models

A. Multipath

Assume that, in the absence of EWF distortion, the received signal, $v(t)+\mu v(t-t_1)+w(t)$, is constituted by a direct ray, a single reflected (multipath) ray and white Gaussian channel noise $w(t)$. The direct ray is $v(t) = A_0 c(t) b(t) \cos(\omega_c t + \omega_d t + \theta_0)$, where $A_0 > 0$ is the amplitude, $c(t)$ and $b(t)$ are, respectively, the code and the data signals, ω_0 is the nominal carrier frequency and ω_d is the Doppler frequency. The reflected ray is characterized by the extra delay t_1 and the multipath parameter μ, which typically takes values in the interval $-1 < \mu < 1$. This allows the reflected ray to have the amplitude $A_0|\mu| < A_0$ and the phase θ_1 equal to θ_0 (inphase) or $\theta_0 + \pi$ (opposite phase).

Consider now specifically the processing of a pilot signal, i.e., $b(t) = 1$. The received signal is heterodyned to baseband using the local carrier $\cos(\omega_c t + \omega_d t)$, yielding $r(t) = s(t) + \mu s(t-t_1) + n(t)$, with $s(t) = A_0 c(t) \cos\theta_0$ and $n(t)$ indicating lowpass noise. The response of the early/late correlators is

$$\begin{bmatrix} I_E(e) \\ I_L(e) \end{bmatrix} = A_0 \begin{bmatrix} R_c\left(e - \Delta_{EL}/2\right) \\ R_c\left(e + \Delta_{EL}/2\right) \end{bmatrix} \cos\theta_0 + \mu A_0 \begin{bmatrix} R_c\left(e - \Delta_{EL}/2 - t_1\right) \\ R_c\left(e + \Delta_{EL}/2 - t_1\right) \end{bmatrix} \cos\theta_1 + \begin{bmatrix} N_E \\ N_L \end{bmatrix} \quad (1)$$

with Δ_{EL} denoting the E-L spacing, e the code discriminator tracking error, $R_c(\cdot)$ the code autocorrelation and $[N_E\, N_L]^T$ is the noise vector. The equilibrium solution for the code discriminator corresponds to the value of e for which the equality $I_L(e) = I_E(e)$ holds.

B. Evil waveform

The threat Model A (TM-A) was originally defined for C/A GPS signals where the positive chips have a falling edge that leads or lags relative to the correct end-time for that chip [8]. This threat model is associated with a failure in the navigation data unit (NDU), the digital partition of the satellite.

The threat model TM-A1 corresponds to the digital distortion (type 1) described in [6]: a lead/lag on every falling transitions after modulation by the code signal. For this model of distortion only one lead/lag parameter, d, is required. Typical waveforms for TM-A1 with BPSK(m) signals and BOCs(m,m) signals are represented in Fig. 1 and Fig. 2, respectively (T_c denotes the chip duration).

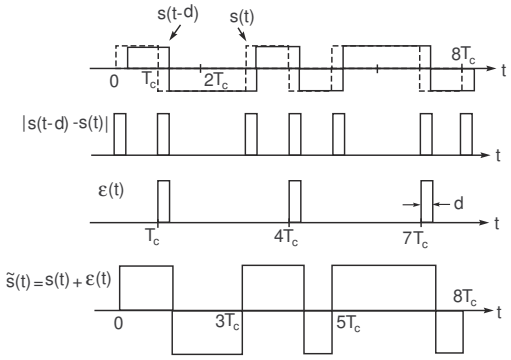

Fig. 1: Typical waveforms for TM-A1 with BPSK(m) signals and $|d| \leq T_c$.

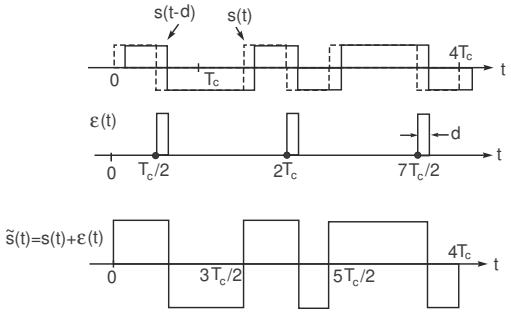

Fig. 2: Typical waveforms for TM-A1 with BOCs(1,1) signals and $|d| \leq T_c$.

The EWF distorted signal is $\widetilde{s}(t) = s(t) + \epsilon(t)$, where the error signal is

$$\epsilon(t) = \frac{1}{2}[s(t-d) - s(t)][1 + \text{sign}\{s(t-d) - s(t)\}] \quad (2)$$

with $\text{sign}(x)$ equal to -1, 0 and $+1$, if $x < 0$, $x = 0$ and $x > 0$, respectively. Defining $q(t) \equiv s(t-d) - s(t)$, we have

$$\epsilon(t)s(t-\tau) = \frac{1}{2}q(t)s(t-\tau) + \frac{1}{2}|q(t)|s(t-\tau). \quad (3)$$

The signals $s(t)$ and $\epsilon(t)$ are periodic random processes with period T (spreading code period). Their means, $E\{s(t)\}$ and $E\{\epsilon(t)\}$, and autocorrelation functions, $R_s(t, t-\tau) \equiv E\{s(t)s(t-\tau)\}$ and $R_\epsilon(t, t-\tau) \equiv E\{\epsilon(t)\epsilon(t-\tau)\}$, depend, in general, on t and τ, and have period T. That is, $E\{s(t+T)\} = E\{s(t)\}$, $R_s(t+T, \tau+T)\} = R_s(t, \tau)$, etc. Consequently, $s(t)$ and $\epsilon(t)$ are cyclostationary processes. For a cyclostationary process, the average cross-correlation function is defined as the average of the cross-correlation function over one period [9]. For instance

$$R_s(\tau) = \langle R_s(t, t-\tau)\rangle = \frac{1}{T}\int_0^T R_s(t, t-\tau)\, dt \quad (4)$$

with $\langle\cdot\rangle$ denoting the time average operator. The (average) power spectral density for a cyclostationary process is defined as $G_s(f) = \mathcal{F}\{R_s(\tau)\}$, with $\mathcal{F}$ denoting the Fourier transform.

In the same way we can define the cross-correlation of $\epsilon(t)$ and $s(t)$ as

$$R_{\epsilon s}(\tau) = \langle s(t)\epsilon(t-\tau)\rangle = \frac{1}{T}\int_0^T R_{\epsilon s}(t, t-\tau)\, dt \quad (5)$$

with T denoting the correlation interval. In the sequel, we obtain by time averaging (3)

$$R_{\epsilon s}(\tau) = \frac{1}{2}R_s(\tau - d) - \frac{1}{2}R_s(\tau) + \frac{1}{2}\langle|q(t)|s(t-\tau)\rangle \quad (6)$$

and

$$\begin{aligned}\langle|q(t)|s(t-\tau)\rangle = \langle q(t)s(t-\tau) \times \text{Prob}\{s(t-d) > s(t)\} \\ - q(t)s(t-\tau) \times \text{Prob}\{s(t-d) < s(t)\}\rangle. \quad (7)\end{aligned}$$

But, for practical codes we have $\text{Prob}\{s(t-d) > s(t)\} \approx \text{Prob}\{s(t-d) < s(t)\}$ and $\langle|q(t)|s(t-\tau)\rangle = 0$. Thus, $R_{\epsilon s}(\tau) = [R_s(\tau - d) - R_s(\tau)]/2$ and the cross-correlation of $\widetilde{s}(t)$ and $s(t)$ is

$$\begin{aligned}R_{\widetilde{ss}}(\tau) &= \langle E\{\widetilde{s}(t)s(t-\tau)\}\rangle = \langle E\{[s(t) + \epsilon(t)]s(t-\tau)\}\rangle \\ &= R_s(\tau) + R_{\epsilon s}(\tau) = \frac{1}{2}\left[R_s(\tau) + R_s(\tau - d)\right]. \quad (8)\end{aligned}$$

The cross-spectrum corresponding to $R_{\widetilde{ss}}(\tau)$ is

$$G_{\widetilde{ss}}(f) = \frac{1}{2}G_s(f)[1 + \exp(-j2\pi fd)] \quad (9)$$

where $G_s(f) = \mathcal{F}\{R_s(\tau)\}$ is the power spectrum of $s(t)$.

Consider now the effect of lowpass filtering the distorted received signal $r(t)$, as shown in Fig. 3, with $H(f)$ indicating the filter transfer function. The filter output is

$$y(t) = r(t) * h(t) = \int_{-\infty}^{\infty} r(\lambda)h(t-\lambda)\, d\lambda \quad (10)$$

where $h(t)$ is the filter impulse response. The correlator output is given by

$$z(\tau) = \frac{1}{T}\int_0^T y(t)g(t-\tau)\, dt \quad (11)$$

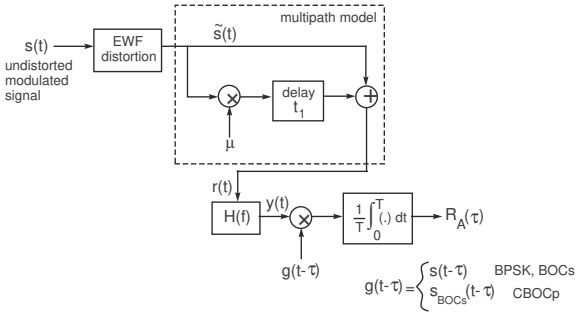

Fig. 3: Cross-correlation of the incoming filtered and distorted signal $y(t)$ and the local non-distorted replica $g(t-\tau)$ for EWF detection.

with the receiver generated signal being

$$g(t-\tau) = \begin{cases} s(t-\tau), & \text{BPSK} \\ s_{BOC}(t-\tau), & \text{BOC, CBOCp.} \end{cases} \tag{12}$$

That is, the correlation is carried out with the distorted and filtered signal and the corresponding locally-generated non-distorted and unfiltered version of the signal but, in the case of transmission of the CBOCpilot signal, we perform instead the correlation with the BOCs(1,1) local carrier with the purpose of simplifying the receiver implementation.

In the following analysis we neglect the effect of the channel noise for the sake of simplicity. The correlator output in Fig. 3 is an instance of the correlation $R_A(\tau) \equiv E\{z(\tau)\}$, where the average $E\{\cdot\}$ is carried out over all the code sequences, with

$$\begin{aligned} R_A(\tau) &= \frac{1}{T}\int_0^T \int_{-\infty}^{\infty} h(t-\lambda) E\{r(\lambda) g(t-\tau)\} d\lambda\, dt \\ &= \frac{1}{T}\int_0^T \int_{-\infty}^{\infty} h(\alpha) R_{\widetilde{sg}}(\tau-\alpha) d\alpha\, dt \\ &+ \frac{\mu}{T}\int_0^T \int_{-\infty}^{\infty} h(\alpha) R_{\widetilde{sg}}(\tau-\alpha-t_1) d\alpha\, dt \\ &= R_{\widetilde{sg}}(\tau) * h(\tau) + \mu R_{\widetilde{sg}}(\tau-t_1) * h(\tau-t_1) \end{aligned} \tag{13}$$

or in the frequency domain

$$G_A(f) = G_{\widetilde{sg}}(f) H(f) [1 + \mu \exp(-j2\pi f t_1)]. \tag{14}$$

Consider that $g(t) = s(t)$. Taking the inverse Fourier transform and using (8) yields

$$\begin{aligned} R_A(\tau) &= \int_{-\infty}^{\infty} G_{\widetilde{ss}}(f) H(f) [1 + \mu \exp(-j2\pi f t_1)] \exp(j2\pi f \tau)\, df \\ &= \frac{1}{2}\int_{-\infty}^{\infty} G_s(f) [1 + \exp(-j2\pi f d)] H(f) \\ &\cdot [1 + \mu \exp(-j2\pi f t_1)] \exp(j2\pi f \tau)\, df. \end{aligned} \tag{15}$$

For the rectangular (ideal) filter of bandwidth B and group delay τ_0 we have

$$H(f) = \begin{cases} \exp(-j2\pi f \tau_0), & |f| < B \\ 0, & \text{otherwise.} \end{cases} \tag{16}$$

Doing $\tau' \equiv \tau - \tau_0$ yields

$$\begin{aligned} R_A(\tau') &= \frac{1}{2}\int_{-B}^{B} G_s(f) \cos(j2\pi f \tau')\, df \\ &+ \frac{1}{2}\int_{-B}^{B} G_s(f) \cos(j2\pi f (\tau' - d))\, df \\ &+ \frac{\mu}{2}\int_{-B}^{B} G_s(f) \cos(j2\pi f (\tau' - t_1))\, df \\ &+ \frac{\mu}{2}\int_{-B}^{B} G_s(f) \cos(j2\pi f (\tau' - d - t_1))\, df. \end{aligned} \tag{17}$$

C. BPSK(m) signals

Define the triangular pulse $\Lambda_L(x - x_0)$ as

$$\Lambda_L(x - x_0) = \begin{cases} 1 - \frac{|x-x_0|}{L}, & |x - x_0| < L \\ 0, & \text{otherwise} \end{cases} \tag{18}$$

with L denoting the pulse half-duration and x_0 its center.

Thus $R_s(\tau) = \Lambda_{T_c}(\tau)$ and $G_s(f) = T_c \operatorname{sinc}^2(fT_c)$, where $T_c = T_{c0}/m$, $m = 1, 2, \ldots$, is the chip duration of the generic BPSK(m) signal, with $T_{c0} = 10^{-3}/1023$ s denoting the chip duration of the GPS C/A code.

Consider $fT_c = x$ (normalized frequency) and $d/T_c = D$ (normalized delay) in (17). We obtain

$$\begin{aligned} R_A(\tau') &= \frac{1}{2}\int_{-BT_c}^{BT_c} \operatorname{sinc}^2(x) \cos\left[2\pi\left(\frac{\tau'}{T_c}\right)x\right] dx \\ &+ \frac{1}{2}\int_{-BT_c}^{BT_c} \operatorname{sinc}^2(x) \cos\left[2\pi\left(\frac{\tau'}{T_c} - D\right)x\right] dx \\ &+ \frac{\mu}{2}\int_{-BT_c}^{BT_c} \operatorname{sinc}^2(x) \cos\left[2\pi\left(\frac{\tau' - t_1}{T_c}\right)x\right] dx \\ &+ \frac{\mu}{2}\int_{-BT_c}^{BT_c} \operatorname{sinc}^2(x) \cos\left[2\pi\left(\frac{\tau' - t_1}{T_c} - D\right)x\right] dx. \end{aligned} \tag{19}$$

Each of the integrals in the previous expression can be expressed by means of the I_{s2c} function [17], which is readily computed in terms of sine integral functions, as described in Appendix A. The use of the I_{s2c} function allows to accelerate the processing speed in semi-analytic simulations and clarifies the role of each of the parameters in the EWF/multipath scenario, such as the normalized bandwidth BT_c or the anomalous level transition delay D.

The resulting expression for (19) is

$$\begin{aligned} R_{A,BPSK}(\tau') &= \frac{1}{2} I_{s2c}\left(1, 2\pi\left(\frac{\tau'}{T_c}\right), BT_c\right) \\ &+ \frac{1}{2} I_{s2c}\left(1, 2\pi\left(\frac{\tau'}{T_c} - D\right), BT_c\right) \\ &+ \frac{\mu}{2} I_{s2c}\left(1, 2\pi\left(\frac{\tau' - t_1}{T_c}\right), BT_c\right) \\ &+ \frac{\mu}{2} I_{s2c}\left(1, 2\pi\left(\frac{\tau' - t_1}{T_c} - D\right), BT_c\right). \end{aligned} \tag{20}$$

When $BT_c \geq 2$ each term of (20) is well approximated by a triangle function spanning $2T_c$.

Fig. 4 exhibits several cross-correlations $R_A(\tau)$ for BPSK(m) modulation and $BT_c = 5$, obtained with multipath and/or EWF effects. The solid lines concern the reception without multipath ($\mu = 0$), the dash-dotted lines correspond to multipath scenarios with $\mu = -0.25$ and the dashed lines correspond to multipath with $\mu = 0.25$. The blue and red lines are associated, respectively, with transmissions with or without EWF distortion ($D = 0.1$ and $D = 0$).

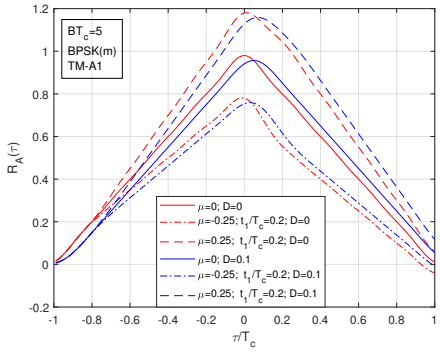

Fig. 4: Cross-correlations $R_A(\tau)$ for BPSK(m) modulation and $BT_c = 5$ with multipath and EWF effects.

D. BOCs(m,m) signals

The autocorrelation function for BOCs signals can be expressed in terms of triangular pulses as [12]

$$R_s(\tau) = \Lambda_{T_c/2}(\tau) - \frac{1}{2}\Lambda_{T_c/2}\left(|\tau| - \frac{T_c}{2}\right) \tag{21}$$

with $\Lambda_L(|x| - x_0) = \Lambda_L(x + x_0) + \Lambda_L(x - x_0)$ denoting two triangles centered at positions $\pm x_0$.

From [12] we have for the power spectrum of the BOCs(m,m) modulation

$$\begin{aligned} G_s(f) &= T_c \operatorname{sinc}^2(fT_c)\tan^2\left(\frac{\pi f T_c}{2}\right) \\ &= \frac{T_c}{2}\operatorname{sinc}^2\left(\frac{fT_c}{2}\right)[1 - \cos(\pi f T_c)]. \end{aligned} \tag{22}$$

Using now (17), with $fT_c = x$ and $d/T_c = D$ and taking into account that $\cos a \cos b = \cos(a+b)/2 + \cos(a-b)/2$, yields

$$\begin{aligned} R_{A,BOC}(\tau') = &\frac{1}{4} I_{s2c}\left(\frac{1}{2}, 2\pi\frac{\tau'}{T_c}, BT_c\right) \\ &- \frac{1}{8} I_{s2c}\left(\frac{1}{2}, \pi\left(1 + 2\frac{\tau'}{T_c}\right), BT_c\right) \\ &- \frac{1}{8} I_{s2c}\left(\frac{1}{2}, \pi\left(1 - 2\frac{\tau'}{T_c}\right), BT_c\right) \\ &+ \frac{1}{4} I_{s2c}\left(\frac{1}{2}, 2\pi\left(\frac{\tau'}{T_c} - D\right), BT_c\right) \\ &- \frac{1}{8} I_{s2c}\left(\frac{1}{2}, \pi\left(1 + 2\frac{\tau'}{T_c} - 2D\right), BT_c\right) \\ &- \frac{1}{8} I_{s2c}\left(\frac{1}{2}, \pi\left(1 - 2\frac{\tau'}{T_c} + 2D\right), BT_c\right) \\ &+ \frac{\mu}{4} I_{s2c}\left(\frac{1}{2}, 2\pi\frac{\tau' - t_1}{T_c}, BT_c\right) \\ &- \frac{\mu}{8} I_{s2c}\left(\frac{1}{2}, \pi\left(1 + 2\frac{\tau' - t_1}{T_c}\right), BT_c\right) \\ &- \frac{\mu}{8} I_{s2c}\left(\frac{1}{2}, \pi\left(1 - 2\frac{\tau' - t_1}{T_c}\right), BT_c\right) \\ &+ \frac{\mu}{4} I_{s2c}\left(\frac{1}{2}, 2\pi\left(\frac{\tau' - t_1}{T_c} - D\right), BT_c\right) \\ &- \frac{\mu}{8} I_{s2c}\left(\frac{1}{2}, \pi\left(1 + 2\frac{\tau' - t_1}{T_c} - 2D\right), BT_c\right) \\ &- \frac{\mu}{8} I_{s2c}\left(\frac{1}{2}, \pi\left(1 - 2\frac{\tau' - t_1}{T_c} + 2D\right), BT_c\right). \end{aligned} \tag{23}$$

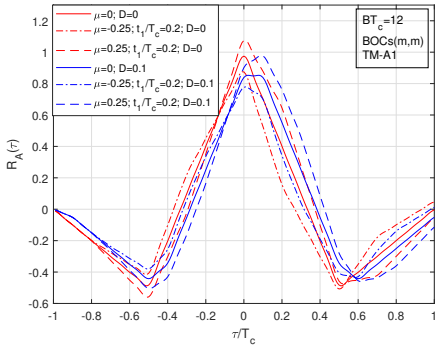

Fig. 5: Cross-correlations $R_A(\tau)$ for BOCs(m,m) modulation and $BT_c = 12$ with multipath and EWF effects.

Fig. 5 exhibits several cross-correlations $R_A(\tau)$ for BOCs(m,m) modulation and $BT_c = 12$, obtained with multipath and/or EWF effects. The black lines concern the reception without multipath ($\mu = 0$) and the blue lines correspond to a multipath scenario ($\mu = 0.25$). The dash-dotted and solid lines are associated, respectively, with transmissions with or without EWF distortion ($D = 0.1$ and $D = 0$). Comparison of Fig. 4 and 5 reveals the differences of the cross-correlation functions $R_A(\tau)$ introduced by the EWF effect. In the BPSK(m) modulation the cross-correlation is shifted rightward by the EWF distortion whereas in the BOCs(m,m) modulation the shift is not apparent: only the rightmost part of the shapes are modified.

E. CBOCpilot signal

The CBOC(6,1,1/11) pilot signal is defined by [13]

$$s_{cboc,p}(t) = [\alpha p_{11}(t) - \beta p_{61}(t)]c(t) = \alpha s_{11}(t) - \beta s_{61}(t) \tag{24}$$

where $\alpha = \sqrt{10/11}$, $\beta = \sqrt{1/11}$, $p_{11}(t)$ is the BOCs(1,1) sub-carrier, $p_{61}(t)$ is the BOCs(6,1) sub-carrier, $c(t)$ is the code signal and $s_{11}(t) = c(t)p_{11}(t)$ is the BOCs(1,1) signal. The receiver correlation scheme is the one sketched in Fig. 3 with the local generator given by $s(t - \tau) = s_{11}(t - \tau)$.

Notice that this correlation scheme is different from those of the BPSK and BOCs modulations, as the signal of the local oscillator is not a replica of the nominal transmitted signal. It is shown in [12] that the power spectrum of the CBOCpilot(6,1,1/11) modulation is given by

$$G_{CBOCp}(f) = \alpha^2 G_{BOCs(1,1)}(f) + \beta^2 G_{BOCs(6,1)}(f) - 2\alpha\beta G_{61,11}(f) \quad (25)$$

with

$$G_{\mathrm{BOCs}(1,1)}(f) = T_c \,\mathrm{sinc}^2(fT_c)\tan^2\left(\frac{\pi f T_c}{2}\right)$$
$$G_{\mathrm{BOCs}(6,1)}(f) = T_c \,\mathrm{sinc}^2(fT_c)\tan^2\left(\frac{\pi f T_c}{12}\right) \quad (26)$$
$$G_{61,11}(f) = \frac{T_c}{36}\,\mathrm{sinc}^2\left(\frac{fT_c}{12}\right)\frac{\sin^2\left(\frac{\pi f T_c}{2}\right)\sin(\pi f T_c)}{\sin\left(\frac{\pi f T_c}{6}\right)}.$$

Using the results in [14] it can be shown that

$$R_{A,CBOCp}(\tau') = \alpha R_{A,BOC}(\tau') - \beta C(\tau') \quad (27)$$

with $R_{A,BOC}(\tau')$ determined by (23) and

$$\begin{aligned} C(\tau') = {} & \frac{1}{144}\sum_{i=1}^{3} I_{s2c2}\left(\frac{1}{12}, \frac{\pi(2i-1)}{6}, 2\pi\frac{\tau'}{T_c}; BT_c\right) \\ & + \frac{1}{144}\sum_{i=1}^{3} I_{s2c2}\left(\frac{1}{12}, \frac{\pi(2i-1)}{6}, 2\pi\left(\frac{\tau'}{T_c} - D\right); BT_c\right) \\ & - \frac{1}{144}\sum_{i=1}^{3} I_{s2c2}\left(\frac{1}{12}, \frac{\pi(2i+5)}{6}, 2\pi\frac{\tau'}{T_c}; BT_c\right) \\ & - \frac{1}{144}\sum_{i=1}^{3} I_{s2c2}\left(\frac{1}{12}, \frac{\pi(2i+5)}{6}, 2\pi\left(\frac{\tau'}{T_c} - D\right); BT_c\right) \\ & + \frac{\mu}{144}\sum_{i=1}^{3} I_{s2c2}\left(\frac{1}{12}, \frac{\pi(2i-1)}{6}, 2\pi\frac{\tau'-t_1}{T_c}; BT_c\right) \\ & + \frac{\mu}{144}\sum_{i=1}^{3} I_{s2c2}\left(\frac{1}{12}, \frac{\pi(2i-1)}{6}, 2\pi\left(\frac{\tau'-t_1}{T_c} - D\right); BT_c\right) \\ & - \frac{\mu}{144}\sum_{i=1}^{3} I_{s2c2}\left(\frac{1}{12}, \frac{\pi(2i+5)}{6}, 2\pi\frac{\tau'-t_1}{T_c}; BT_c\right) \\ & - \frac{\mu}{144}\sum_{i=1}^{3} I_{s2c2}\left(\frac{1}{12}, \frac{\pi(2i+5)}{6}, 2\pi\left(\frac{\tau'-t_1}{T_c} - D\right); BT_c\right). \end{aligned} \quad (28)$$

The function $I_{s2c2}(\cdot)$ is described in Appendix B. Fig. 6 exhibits the receiver cross-correlations $R_A(\tau')$ for CBOC pilot signals with $BT_c = 12$ and with or without multipath and EWF effects. As expected, Figs. 5 and 6 are similar. In fact, when the CBOCpilot signals are processed with a lowpass filter with normalized bandwidth $BT_c = 12$, the high-frequency components, corresponding to the modulation BOCs(6,1), are practically filtered out.

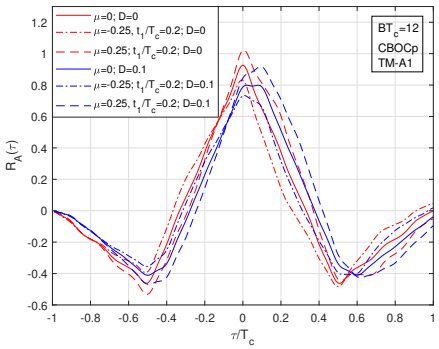

Fig. 6: Cross-correlations $R_A(\tau)$ for CBOCpilot modulation and $BT_c = 12$ with multipath and EWF effects.

III. Signal Quality Monitoring

Signal Quality Monitoring (SQM) is a set of algorithms that allow to detect the threatening EWF distortions in the code autocorrelation function. The SQM is necessary to protect users with high requirements in terms of integrity, accuracy, availability, and continuity, such as civil aviation users [3].

To improve the reliability of the SQM mechanism, multiple combinations of pairs of correlators can be used with simple ratio, difference ratio and sum ratio metrics. This requires that the receiver includes a bank of $2N+1$ correlators, with N pairs of early/late correlators plus a prompt correlator, as sketched in Fig. 7. In the figure $r(t)$ is the received signal containing the GNSS signal of power P and additive white Gaussian noise of power spectral density $N_0/2$. The separation Δ between correlators is typically lower-bounded by ≈ 10 ns because lower values require sampling rates above 100 MHz, which is more difficult to achieve by the ADCs.

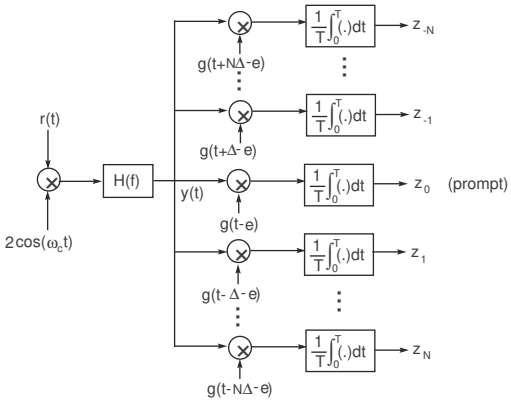

Fig. 7: EWF detector using a bank of correlators.

The correlator outputs in the scheme of Fig. 7 are

$$Z_i = \sqrt{2P}R_A(e - i\Delta) + n_i, \quad i = 0, \pm 1, \cdots, \pm N \quad (29)$$

where the noises n_i are correlated, zero-mean, Gaussian random variables, with common variance $E\{n_i^2\} = (N_0/T)R_g(0)$, with $R_g(\tau)$ denoting the autocorrelation

of $g(t)$. The cross-correlations between the noises are $E\{n_i n_k\} = (N_0/T)R_g((i-k)\Delta)$.

SQM consists of one or more tests to determine if the incoming signal is affected by EWF distortion or not. The two hypotheses are H_0 (non-distorted signal) and H_1 (distorted signal). For a given metric M let $\mathcal{T}$ denote the test variable generically defined by

$$\mathcal{T} = (M_{\text{mea}} - M_{\text{nom}})/\lambda \tag{30}$$

where M_{mea} is the measured value of the metric, which is disturbed by thermal noise and may or not be affected by signal distortion (anomaly), and M_{nom} is the nominal value of the metric (no additive noise or distortion). Typically, the random variable $\mathcal{T}$ has Gaussian distribution with zero mean for hypothesis H_0. Parameter λ is used to adjust the variance of $\mathcal{T}$, such that $\text{Prob}\{\mathcal{T} \geq 1|H_0\} = P_{fa}$, where P_{fa} is the desired probability of false alarm.

To detect EWF distortion, the test variable $\mathcal{T}$ is compared to the unity decision threshold: if $\mathcal{T} < 1$ hypothesis H_0 is considered, otherwise hypothesis H_1 is assumed. The probability of missing detection is defined as $P_{md} = \text{Prob}\{\mathcal{T} < 1|H_1\}$. It is not possible to minimize simultaneously P_{fa} and P_{md} by shifting the unity decision threshold, as illustrated in Fig. 8. An workable solution is the Neyman-Pearson criterion which consists of fixing P_{fa} at a preselected value, by adjusting parameter λ. Then, for each EWF scenario a different value of P_{md} is obtained [15].

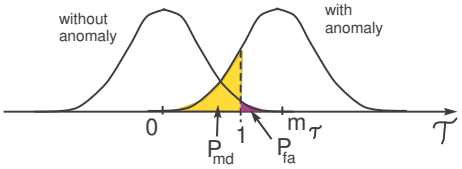

Fig. 8: Probabilitiy density functions of test variable $\mathcal{T}$ with and without signal anomaly.

In [3], three tests based on different ratio metrics were proposed. The metrics considered are: simple ratio metric, difference ratio metric and sum ratio metric. Associated with those metrics we build tests T_1, T_2 and T_3, respectively.

A. Simple ratio test (T1 test)

With $2N+1$ correlators we can form $2N$ simple ratio metrics

$$M_1^{(i)} = Z_i/Z_0, \quad i = \pm 1, \ldots, \pm N \tag{31}$$

and the corresponding test variables $\mathcal{T}_1^{(i)}$, according to (30). These variables are used to build a decision criterion, where we assume hypothesis H_1 if, at least, one pair of correlators verifies $\mathcal{T}_1^{(i)} > 1$. The overall probability of false alarm is then given by

$$\begin{aligned} P_{FA} &= \text{Prob}\{\bigcup_{\substack{i=-N \\ i\neq 0}}^{N} \mathcal{T}_1^{(i)} \geq 1|H_0\} \\ &= 1 - \text{Prob}\{\bigcap_{\substack{i=-N \\ i\neq 0}}^{N} \mathcal{T}_1^{(i)} < 1|H_0\} \end{aligned} \tag{32}$$

where $\bigcup$ and $\bigcap$ mean, respectively, the union and the intersection of events. It can be shown [16] that the normalization parameters $\lambda_1^{(i)}$ are given by

$$\lambda_1^{(i)} = \frac{\text{erfc}^{-1}(P_{FA}/(2N))}{R_A(0)} \sqrt{\frac{(1+\rho_i^2)R_s(0) - 2\rho_i R_s(i\Delta)}{(C/N_0)T}} \tag{33}$$

with $\rho_i \equiv R_A(i\Delta)/R_A(0)$, $i \neq 0$. The overall probability of missing detection is

$$P_{MD} = \text{Prob}\{\bigcap_{\substack{i=-N \\ i\neq 0}}^{N} \mathcal{T}_1^{(i)} < 1|H_1\}. \tag{34}$$

B. Difference ratio test (T2 test)

With N pairs of early/late correlators we can form N difference ratio metrics

$$M_2^{(i)} = (Z_{-i} - Z_i)/Z_0, \quad i = 1, \ldots, N. \tag{35}$$

and the corresponding test variables $\mathcal{T}_2^{(i)}$. The overall probability of false alarm is given by

$$P_{FA} = 1 - \text{Prob}\{\bigcap_{\substack{i=-N \\ i\neq 0}}^{N} |\mathcal{T}_2^{(i)}| < 1|H_0\} \tag{36}$$

and the overall probability of missing detection is

$$P_{MD} = \text{Prob}\{\bigcap_{\substack{i=-N \\ i\neq 0}}^{N} |\mathcal{T}_2^{(i)}| < 1|H_1\} \tag{37}$$

The normalization parameters $\lambda_2^{(i)}$ are [16]

$$\lambda_2^{(i)} = \frac{\sqrt{2}\,\text{erfc}^{-1}(P_{FA}/N)}{R_A(0)} \sqrt{\frac{R_s(0) - R_s(2i\Delta)}{(C/N_0)T}}. \tag{38}$$

C. Sum ratio test (T3 test)

With N pairs of early/late correlators we can also form N difference ratio metrics

$$M_3^{(i)} = (Z_{-i} + Z_i)/Z_0, \quad i = 1, \ldots, N. \tag{39}$$

and the corresponding test variables $\mathcal{T}_3^{(i)}$. The overall probability of false alarm and missing detection are given, respectively, by (32) and (34) with $\mathcal{T}_1^{(i)}$ replaced by $\mathcal{T}_3^{(i)}$. The normalization parameters $\lambda_3^{(i)}$ are [16]

$$\begin{aligned} \lambda_3^{(i)} &= \frac{\sqrt{2}\,\text{erfc}^{-1}(2P_{FA}/N)}{R_A(0)} \\ &\times \sqrt{\frac{R_s(0) + R_s(2i\Delta) - 2R_s^2(i\Delta)/R_s(0)}{(C/N_0)T}}. \end{aligned} \tag{40}$$

IV. Simulation results

In this section we present Monte Carlo simulation results for tests T1, T2 and T3, obtained in the presence of multipath: a direct ray plus one reflected ray with relative delay t_1/T_c and normalized amplitude μ. In order to permit the determination of the robustness of EWF detectors to the presence of multipath, we plot in Fig. 9 the curves of the overall probabilities of missing detection versus D for the modulations BPSK(m), BOCs(m,m) and CBOCpilot when no multipath is present ($\mu = 0$). We have considered $N = 4$, $\Delta = 0.02\,T_c$, $BT_c = 12$, $(C/N_0) = 50$ dB-Hz and $T = 20$ ms. The figure shows that for all the tests the EWF detectors have the best performance with CBOCpilot signals and the worse performance with BPSK(m) signals. In general, the best performing test is T3, as it requires the smallest values of EWF parameter D to achieve, for instance, $P_{MD} = 10^{-3}$. Test T2 fails to detect the presence of EWF distortion for all reasonable values of D. As a consequence, we will discard test T2 in the following assessment of test performance. Note, also, that the results herein obtained for T1 and T3 tests must be treated with caution as they may not hold for more complicated multipath scenarios, constituted, for instance, by a larger number of reflectors.

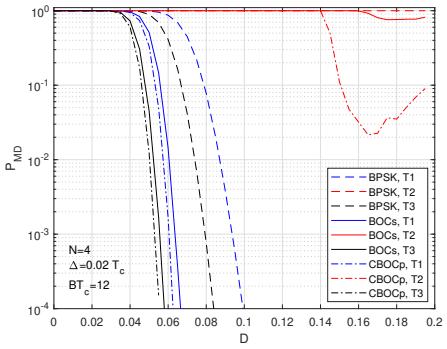

Fig. 9: Probabilities of EWF missing detection for different tests and modulations in a scenario without multipath versus the EWF parameter D.

Figs. 10 and 11 present the probabilities of EWF missing detection, respectively for tests T1 and T3, with different modulations, in a scenario with multipath: $t_1/T_c = 0.1$ and $\mu = \pm 0.25$. The performance of BPSK(m,m) for $\mu = 0.25$ is unacceptable with both tests. Besides, for CBOCpilot and $\mu = -0.25$ the results are unacceptable when using test T3 and $D \geq 0.18$. Test T3 was repeated in Fig. 12 but with $N = 6$. The existing degradation for CBOCpilot disappeared but the performance of the BPSK(m,m) remains poor. Therefore, only modulations BOCs(m,m) and CBOCpilot can provide conveniently low values of P_{MD} for $D \geq 0.07$.

The performance of tests T1 and T3 in terms of false alarm (multipath present but no EWF) is displayed in Figs. 13 and 14 for BPSK(m), in Figs. 15 and 16 for BOCs(m,m), and in Figs. 17 and 18 for CBOCpilot. The white regions of the plots correspond to $P_{FA} < 10^{-4}$ and the various levels of probability are indicated by $\log_{10}(P_{FA})$. Except for small

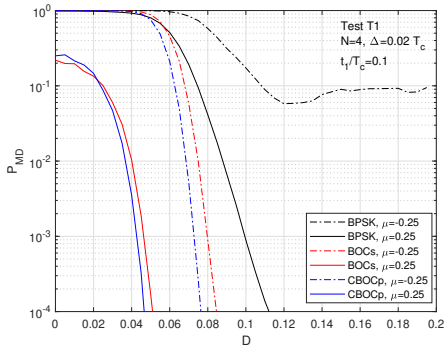

Fig. 10: Probabilities of EWF missing detection for test T1 with different modulations in a scenario with multipath versus the EWF parameter D.

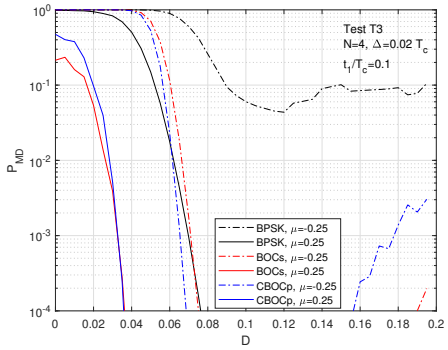

Fig. 11: Probabilities of EWF missing detection for test T3 with $N = 4$ and different modulations in a scenario with multipath versus the EWF parameter D.

amplitudes of the reflected ray ($|\mu| \leq 0.05$), all the values of P_{FA} are unacceptably high regardless of the values of the normalized multipath delay t_1/T_c. The different extensions of the colored regions for tests T1 and T3 show that, globally, T3 outperforms T1. Notice the asymmetry of the figures relative to $\mu = 0$; this means that the probability of false alarm depends

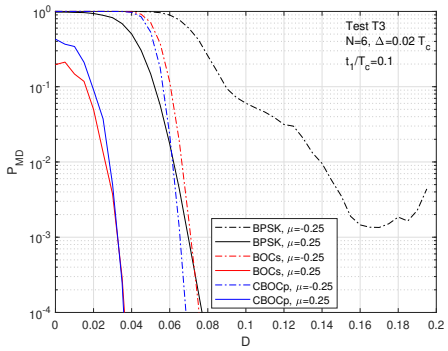

Fig. 12: Probabilities of EWF missing detection for test T3 with $N = 6$ and different modulations in a scenario with multipath versus the EWF parameter D.

also on the sign of the multipath intensity μ.

The figures reveal that the EWF detection techniques under analysis are very sensitive to the presence of multipath. This fact was expected as multipath and EWF anomalies, although being generated by entirely independent mechanisms, provoke similar distortions in the autocorrelation function of the received signals, as evidenced by eqs. (20), (23) and (27)-(28). Since the probability of false alarm is more significantly affected by multipath than the probability of missing detection, a possible solution to the problem of multipath interference consists of making a decision based on a set of m monitoring stations located at separate places, such that the multipath effect in each one is independent from the others. The following decision criterion could then be applied: an EWF anomaly is declared present if the m receivers detect *simultaneously* the presence of the anomaly.

In each receiver the false alarm results from the contribution of two independent mechanisms: channel noise and multipath, with probabilities respectively equal to P_{FA} and P_{mult}. Assuming a typical scenario with $P_{\text{mult}} \gg P_{FA}$, then the probability of false alarm in the presence of multipath and thermal noise is $P'_{FA} \approx P_{\text{mult}}$. For that scenario, the overall probability of false alarm for the m receivers is given by the probability of the following intersection of independent events

$$\widetilde{P}_{FA} = \text{Prob}\{z_1 > V_{\text{th}},\, z_2 > V_{\text{th}}, \ldots, z_m > V_{\text{th}} | H_0\} \quad (41)$$

where z_i is the decision random variable (r.v.) in receiver i and V_{th} is the decision threshold (adjusted to the case of no multipath and no EWF). Since $z_1,\, z_2, \ldots$ are independent r.v. we obtain

$$\widetilde{P}_{FA} = \prod_{i=1}^{m} \text{Prob}\{z_i > V_{\text{th}}\} = (P'_{FA})^m \approx P_{\text{mult}}^m. \quad (42)$$

That is, using the m independent receivers the overall probability of false alarm will be much smaller than P_{mult}. For instance, assuming that $P_{\text{mult}} = 0.2$ and using $m = 6$ receivers yields $\widetilde{P}_{FA} \approx 6.4 \times 10^{-5}$.

As for the overall probability of missing detection we have

$$\widetilde{P}_{MD} = 1 - \text{Prob}\{z_1 > V_{\text{th}},\, z_2 > V_{\text{th}}, \ldots, z_m > V_{\text{th}} | H_1\} \quad (43)$$

where $z_i = A + \rho_i + n_i$. A is a positive quantity that depends on the EWF, ρ_i is a zero-mean r.v. due to the multipath and n_i is a zero-mean Gaussian r.v. with variance σ_n^2 depending on the thermal noise. Thus

$$\begin{aligned} \widetilde{P}_{MD} &= 1 - \prod_{i=1}^{m} \text{Prob}\{n_i > V_{\text{th}} - A - \rho_i\} \\ &= 1 - \prod_{i=1}^{m} Q\left(\frac{V_{\text{th}} - A - \rho_i}{\sigma_n}\right) \end{aligned} \quad (44)$$

with $Q(\cdot)$ denoting the error function

$$Q(x) = \frac{1}{\sqrt{2\pi}} \int_x^{\infty} \exp(-y^2/2)\, dy. \quad (45)$$

Fig. 19 displays the values of $\widetilde{P}_{\text{MD}}$ versus the number m of receivers for different intensities S of multipath, obtained with Monte Carlo simulation. It is considered that $A = V_{\text{th}} + 3.08$, which corresponds to $\widetilde{P}_{\text{MD}} = 10^{-3}$ when $m = 1$ and multipath is absent ($\rho_1 = 0$). The quantities ρ_i are modeled as independent zero-mean uniformly distributed r.v. in the interval $-S/2 \leq \rho_i \leq S/2$, with the case $S = 0$ referring to the scenario without multipath. The figure shows that, for every value of the multipath intensity S, the overall probability of missing detection increases linearly with the number of receivers, whereas the overall probability of false alarm is shown in (42) to decrease with a power of exponent m.

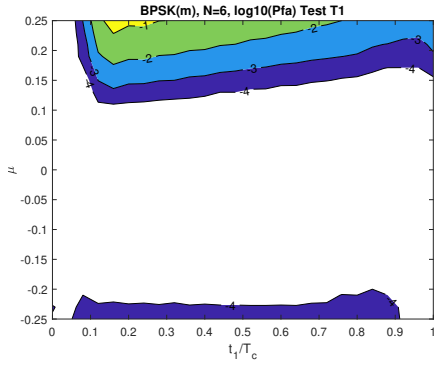

Fig. 13: Probabilities of false alarm for test T1 and BPSK(m) versus the multipath delay t_1/T_c (white region: $P_{FA} < 10^{-4}$).

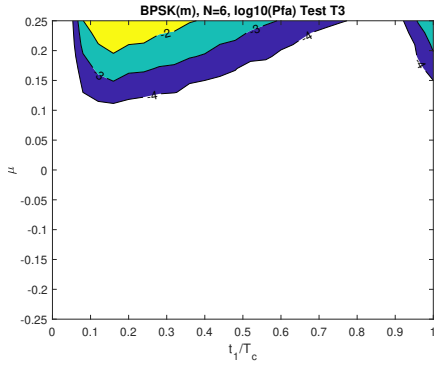

Fig. 14: Probabilities of false alarm for test T3 and BPSK(m) versus the multipath delay t_1/T_c.

V. Conclusion

Detection of evil waveforms (EWF) in GNSS is an important way to avoid the use of anomalous signals that could degrade the accuracy of the PVT solution. EWF detectors are usually based on the determination of asymmetries and other type of distortions that occur in the code autocorrelation function of the received signals due to malfunction of the satellite equipment. However, similar distortions are obtained with healthy signals in multipath scenarios, making the distinction between EWF and multipath very difficult.

In this work we analyzed the effect of multipath on the performance of EWF detectors, having concluded that the probability of false alarm in a multipath scenario with no

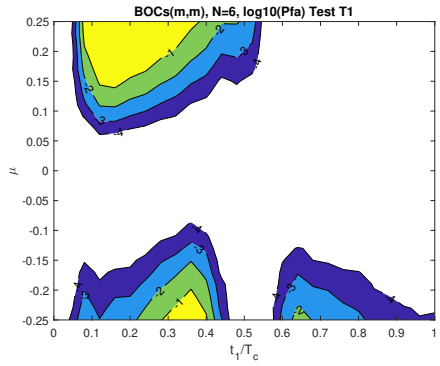

Fig. 15: Probabilities of false alarm for test T1 and BOCs(m,m) versus the multipath delay t_1/T_c.

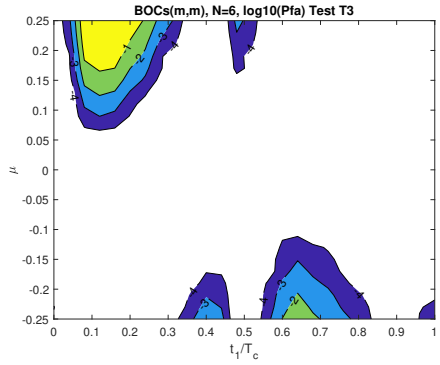

Fig. 16: Probabilities of false alarm for test T3 and BOCs(m,m) versus the multipath delay t_1/T_c.

EWF is prone to increase by an unacceptable amount and the probability of missing detection is also aggravated, although in a smaller scale. This suggests a solution to mitigate the problem that resorts to a set of independent receivers located in separate places. The idea is to make use of the fact that multipath is a local effect, contrarily to the EWF anomaly, which is a global effect. As a result, making decisions based on the whole set of receivers produces a significant decrease of the probability of false alarm with only a fair increase in the probability of missing detection.

Due to the lack of space only the TM-A1 model was analyzed herein. Suggested future work includes the analysis of the remaining threat models. The assumed multipath model scenario, which is constituted by a direct and a reflected ray is, of course, overly simplistic, and in future research more realistic statistical multipath models should be considered.

Appendix A
Computation of Integral I_{s2c}

The integral is defined as

$$I_{s2c}(a,b;L) \equiv \int_{-L}^{L} \mathrm{sinc}^2(ax)\cos(bx)\,dx \tag{46}$$

with $\mathrm{sinc}(x) \equiv \sin(\pi x)/(\pi x)$. But $\sin^2 x = (1-\cos(2x))/2$. Thus

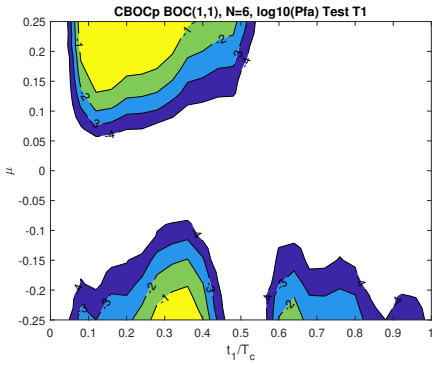

Fig. 17: Probabilities of false alarm for test T1 and CBOCpilot versus the multipath delay t_1/T_c.

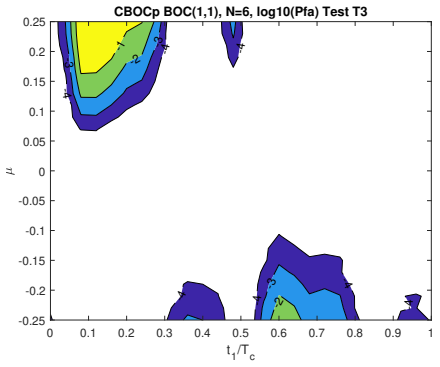

Fig. 18: Probabilities of false alarm for test T3 and CBOCpilot versus the multipath delay t_1/T_c.

$$I_{s2c}(a,b;L) = \frac{1}{2\pi^2 a^2}\int_{-L}^{L}\frac{\cos(bx)}{x^2}\,dx - \frac{1}{2\pi^2 a^2}\int_{-L}^{L}\frac{\cos(2\pi a x)\cos(bx)}{x^2}\,dx. \tag{47}$$

Since $\cos a \cos b = [\cos(a+b)+\cos(a-b)]/2$, we have

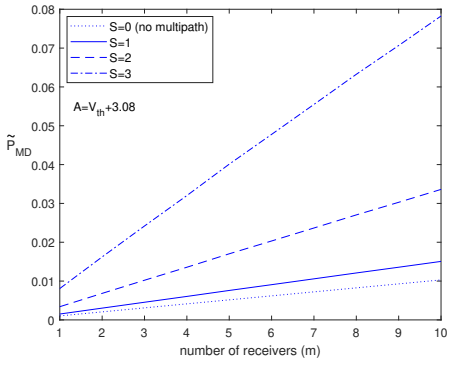

Fig. 19: Overall probabilities of missing detection versus the number of receivers with different intensities of multipath.

$$I_{s2c}(a,b;L) = \frac{1}{4\pi^2 a^2}\int_{-L}^{L}\frac{\cos(bx)-\cos[(2\pi a+b)x]}{x^2}\,dx + \frac{1}{4\pi^2 a^2}\int_{-L}^{L}\frac{\cos(bx)-\cos[(2\pi a-b)x]}{x^2}\,dx. \quad (48)$$

It is known that [11] (3.784)

$$\int_{-\infty}^{\infty}\frac{\cos(\alpha x)-\cos(\beta x)}{x^2}\,dx = \pi(|\beta|-|\alpha|) \quad (49)$$

and

$$\int_{L}^{\infty}\frac{\cos(\mu x)}{x^2}\,dx = -\frac{\pi|\mu|}{2}+\mu \mathrm{S_i}(\mu L)+\frac{\cos(\mu L)}{L}, \quad L>0 \quad (50)$$

where $\mathrm{S_i}(\cdot)$ is the sine integral function [10]. Define now the integral

$$I_{cc}(\alpha,\beta;L) \equiv \int_{-L}^{L}\frac{\cos(\alpha x)-\cos(\beta x)}{x^2}\,dx \quad (51)$$

which can be simplified to

$$I_{cc}(\alpha,\beta;L) = 2\left[\beta \mathrm{S_i}(\beta L)+\frac{\cos(\beta L)}{L}-\alpha \mathrm{S_i}(\alpha L)-\frac{\cos(\alpha L)}{L}\right]. \quad (52)$$

Using (52) in (48) leads to

$$I_{s2c}(a,b;L) = \frac{1}{4\pi^2 a^2}\left[I_{cc}(b,2\pi a+b;L)+I_{cc}(b,2\pi a-b;L)\right]. \quad (53)$$

This result permits to compute the integral $I_{s2c}(a,b;L)$ in terms of trigonometric and sine integral functions.

From (49) and (53) it can be shown that the asymptotic value for the integral I_{s2c} is the triangle function

$$\lim_{L\to\infty} I_{s2c}(a,b;L) = \frac{1}{a}\Lambda_{2\pi a}(b), \quad a>0. \quad (54)$$

Fig. 20 displays the function $I_{s2c}(1,b;L)$ versus b for different values of L. Note that, for $L \geq 2$, the function is well approximated by a triangle spanning 2π with unity height.

APPENDIX B
COMPUTATION OF INTEGRAL I_{s2c2}

The integral is defined as

$$I_{s2c2}(a,b,c;L) \equiv \int_{-L}^{L}\mathrm{sinc}^2(ax)\cos(bx)\cos(cx)\,dx \quad (55)$$

and can be written in terms of the integrals I_{s2c} as

$$I_{s2c2}(a,b,c;L) = \frac{1}{2}\int_{-L}^{L}\mathrm{sinc}^2(ax)\cos[(b+c)x]\,dx + \frac{1}{2}\int_{-L}^{L}\mathrm{sinc}^2(ax)\cos[(b-c)x]\,dx \quad (56)$$

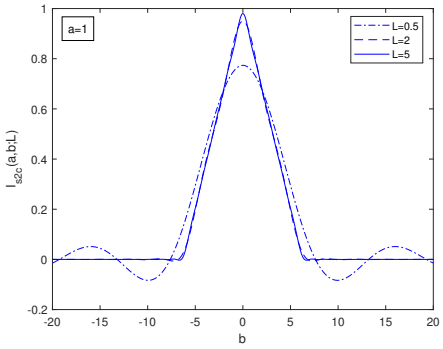

Fig. 20: Plot of function $I_{s2c}(a,b;L)$ versus b for $a=1$ and different values of L.

or

$$I_{s2c2}(a,b,c;L) = \frac{1}{2}[I_{s2c}(a,b+c;L)+I_{s2c}(a,b-c;L)]. \quad (57)$$

REFERENCES

[1] R. Phelts, "Multicorrelator techniques for robust mitigation of threats to GPS signal quality," PhD Thesis, Stanford University, June 2001.

[2] P. Thevenon, O. Julien, Q. Tessier, D. Maillard, M. Cabantous, F. Amarillo-Fernández, and F. Oliveira-Salgueiro, "Detection performances of evil waveform monitors for the GPS L5 signal", ION GNSS+ 2014, pp. 3312–3322, Tampa, FL, September 2014.

[3] J. Pagot,"Modeling and monitoring of new GNSS signal distortions in the context of civil aviation", PhD Thesis, MITT, Toulouse, France, December 2016.

[4] I. Selmi, P. Thevenon, C. Macabiau, J. Olivier, and M. Mabilleau, "Signal quality monitoring algorithm applied to Galileo signals for large evil waveform threat space", ION ITM 2020, pp. 352-365, San Diego, CA, January 2020.

[5] M. Vergara, F. Antreich, C. Enneking, M. Sgammini, and G. Seco-Granados, "A model for assessing the impact of linear and nonlinear distortions on a GNSS receiver", GPS Solutions, vol. 24(5), pp. 1-18, 2020.

[6] J. Pagot, P. Thevenon, O. Julien, F. A. Fernandez, D. Maillard, "Threat model design for new GNSS signals", ION ITM 2016, pp. 970-982, Monterey, CA, January 2016, pp. 970-982.

[7] J. Pagot, P. Thevenon, O. Julien, F. A. Fernandez, D. Maillard, "Signal quality monitoring for new GNSS signals", ION GNSS+, Portland, OR, September 2016, pp. 1750-1763.

[8] "ICAO - Annex 10: Aeronautical telecommunications - Volume 1: Radio navigation aids", July 2018.

[9] J. Proakis and M. Salehi, Digital Communications, fifth edition, Boston: McGraw-Hill, 2008.

[10] M. Abramowitz and I. Stegun (edts), Handbook of Mathematical Functions, N. York: Dover, 1970.

[11] I. S. Gradshteyn and I. M. Ryzhik, Table of Integrals, Series, and Products, S. Diego, CA: Academic Press, 1980.

[12] F. Sousa, F. Nunes, "New expressions for the autocorrelation function of BOC GNSS signals", Navigation, vol. 60(1), 2013, pp. 1-9.

[13] European GNSS (Galileo) Open Service, "Signal-in-Space interface control document", Issue 2.0, European Union, January 2021.

[14] A. Negrinho, P. Fernandes, P. Boto, F. Nunes, F. Sousa, "Evil Waveforms Detection Solutions for Autonomous Navigation Integrity", ION GNSS+, September 2021, pp. 4097-4115.

[15] S. Kay, Fundamentals of Statistical Signal Processing. Detection Theory. Vol. II, N. York: Prentice Hall, 1998.

[16] F. Sousa, F. Nunes, A. Negrinho, P. Fernandes, P. Boto, "Signal Quality Monitoring Aspects in GNSS Signals Affected by Evil Waveforms", ESA Navitec 2022.

[17] F. Nunes, F. Sousa, "Analysis of Threat Models", project Monint, ESA/GMV/IT, unpublished, 2021.